

Physics-Based Low-Order Model for Transonic Flutter Prediction

Max M. J. Opgenoord*, Mark Drela[†] and Karen E. Willcox[‡]

Massachusetts Institute of Technology, Cambridge, MA, 02139

This paper presents a physical low-order model for two-dimensional unsteady transonic airfoil flow, based on small unsteady disturbances about a known steady flow solution. This is in contrast to traditional small-disturbance theory which assumes small disturbances about the freestream. The states of the low-order model are the flowfield's lowest moments of vorticity and volume-source density perturbations, and their evolution equations coefficients are calibrated using off-line unsteady CFD simulations through dynamic mode decomposition. The resulting low-order unsteady flow model is coupled to a typical-section structural model, thus enabling prediction of transonic flutter onset for moderate to high aspect ratio wings. The method is fast enough to permit incorporation of transonic flutter constraints in conceptual aircraft design calculations. The accuracy of this low-order model is demonstrated for forced pitching and heaving simulations of an airfoil in compressible flow. Finally, the model is used to describe the influence of compressibility on the flutter boundary, and its accuracy is demonstrated for the Isogai Case A classical flutter test case.

Nomenclature

\mathbf{A}, \mathbf{E}	State-space matrices	k_h	Spring constant for vertical motion
$\mathbf{A}_a, \mathbf{B}_a$	State-space matrices of aerodynamic system	k_θ	Torsional spring constant
$A_\Gamma, A_{\dot{\Gamma}}, A_\kappa$	Coefficients of Γ evolution equation	m	Mass
$B_\Gamma, B_{\dot{\Gamma}}, B_{\dot{\kappa}}$	Coefficients of κ_x evolution equation	$\hat{\mathbf{n}}$	Normal unit vector
D_{wave}	Wave drag	\mathbf{r}	Position vector
I_θ	Moment of inertia around elastic axis	r_θ	Radius of gyration about the airfoil's elastic axis
L	Lift	t	Time
M_{crit}	Critical Mach number	\mathbf{u}	State-space control vector
M_∞	Free stream Mach number	\mathbf{u}_a	State-space control vector of aerodynamic system
S_θ	Mass unbalance	w	Vertical velocity, positive downward
\mathbf{V}	Velocity field	\mathbf{x}	State-space vector
\mathbf{V}_0	Velocity field of steady solution	x, z	Physical coordinates along freestream
V_μ	Flutter speed index	\mathbf{x}_a	State-space vector of aerodynamic system
\mathbf{V}_∞	Free stream velocity	x_{cg}	Position of center of gravity relative to leading edge
X, X', X''	Matrices containing sequences of snapshots of state vector	x_{ea}	Position of elastic axis relative to leading edge
a	Local speed of sound		
a, a_l, b	Discrete state-space matrices		
c	Airfoil chord length		
c_ℓ	Lift coefficient		
d	Distance between quarter-chord and elastic axis	<i>Symbols</i>	
h	Vertical position, positive downward	α	Angle of attack
		Γ	Circulation strength

*Graduate student, Department of Aeronautics and Astronautics, mopg@mit.edu, Student Member AIAA

[†]Terry J. Kohler Professor of Aeronautics and Astronautics, Department of Aeronautics and Astronautics, drela@mit.edu, Fellow AIAA

[‡]Professor of Aeronautics and Astronautics, kwillcox@mit.edu, Associate Fellow AIAA

θ	Pitch angle	ϕ	Velocity potential
κ_x	x -doublet strength	ω	Vorticity
μ	Apparent mass ratio	ω	Angular velocity
ρ_∞	Free stream density	$\bar{\omega}$	Reduced frequency
σ	Volume-source strength	ω_θ, ω_h	Uncoupled in-vacuo natural frequencies in pitch and heave
Υ'	Matrix containing sequence of snapshots of control input vector		

I. Introduction

THE push for more efficient transport aircraft leads to larger wing spans and more flexible wings, configurations for which flutter becomes a significant design consideration. This is especially true for next-generation airplane concepts, such as the Truss-Braced Wing.¹ However, incorporating flutter prediction into early-stage design is a considerable challenge for the transonic flow regime relevant to most civil transport aircraft designs, since existing accurate models for transonic flutter prediction typically require extensive computational fluid dynamic (CFD) analyses that are too expensive to conduct in early design stages where potentially thousands of wing designs might be considered. Flutter constraints can be included in state-of-the-art multidisciplinary design optimization settings, but even if the static aeroelastic methods are high fidelity, the methods for unsteady (compressible) flow usually either linearize the unsteady response or use a Prandtl-Glauert correction,^{2,3} which is limited to subsonic flow. In this paper, we develop an accurate, fast, low-order model for small-amplitude transonic unsteady airloads, intended for flutter prediction in early-stage design and optimization of transport aircraft.

While flutter for low subsonic flows can, in general, be accurately predicted with linearized small-disturbance theories, they fail for transonic flow where the traditional small-disturbance formulation is inherently nonlinear.⁴ For example, linear theory predicts that thinner wings would be less susceptible to flutter, but wind tunnel tests have shown the opposite to be true.⁴ Another interesting phenomenon that occurs in transonic flows is the transonic dip in the flutter boundary.⁵⁻⁸ Linear theories cannot predict the location or shape of the transonic dip, and tend to produce optimistic estimates for the flutter boundary.⁹

The seminal work by Theodorsen¹⁰ is widely used for incompressible flutter predictions for two-dimensional airfoils. Several researchers extended Theodorsen's theory to subsonic flows,¹¹⁻¹³ with none of these methods extending to the transonic regime. Moreover, Theodorsen theory is only strictly valid for simple harmonic motion, which strictly applies only at the flutter boundary.

Possio¹⁴ applied the acceleration potential to a two-dimensional subsonic compressible nonstationary problem and arrived at an integral equation (Possio's equation) for subsonic unsteady compressible flow. Closed-form solutions to an approximation of Possio's equation were found in 1999.^{15,16} However, the accuracy for Possio's method deteriorates for transonic flows and for high-frequency oscillations.¹⁷ Lomax et al.¹⁸ used piston theory to analytically find the lift response to unsteady perturbations in subsonic flow, but only for the non-circulatory part of the lift. Stahara and Spreiter,¹⁹ Isogai,²⁰ and Dowell²¹ developed models for linearized transonic flow, applicable to thin airfoils in shock-free flows. A linearization of the Transonic Small-Disturbance (TSD) equation for unsteady transonic flow was first proposed by Nixon,²² which involves changing the airfoil geometry for transonic flows such that the shock location does not change during any perturbations.

These analytical/theoretical methods all suffer from a loss of accuracy in transonic flows with shocks on the airfoil surface, which are typical on jet transports. Other approaches have attempted to address this limitation by deriving models using a combination of theory and experimental data, as in the work of Leishman and Nguyen²³ who formulated a state-space representation of unsteady airfoil behavior with some parameters estimated from experimental data, or by deriving reduced-order models from high-fidelity CFD models. A reduced-order modeling approach starts with the full state (flow field) information collected from a CFD solver and identifies a low-dimensional subspace in which the most important system dynamics evolve.²⁴ Methods such as the harmonic balance,²⁵ proper orthogonal decomposition,²⁶⁻²⁸ and Volterra series²⁹ have all been used to derive aeroelastic reduced-order models.³⁰ These methods have been applied in practice successfully, amongst others, for unsteady transonic flow around full wings,³¹ a full F-16 aircraft configuration,³² and many more.

In contrast to the reduced-order modeling approach, which starts with a high-order model and reduces the state by pure numerics, our work constructs a *physics-based low-order model* a priori, in terms of

the flowfield’s volume-source and vorticity moments. Our state variables are the unsteady perturbations of these moments from some known steady transonic solution, and their time evolution is governed by postulated equations whose coefficients are treated as parameters. These parameters are calibrated using high-fidelity CFD results. Our underlying assumption is that the baseline steady flow is statically nonlinear, but sufficiently small disturbances around the baseline solution can be assumed to produce a linear response in the overall volume-source and vorticity moments.³³ The resulting model produces unsteady perturbation lift and moment outputs, which can be combined with a conventional typical-section structural elastic model to obtain an overall aeroelastic state-space model suitable for flutter prediction.

We develop the present aerodynamic model as an extension of the one used in ASWING,^{34,35} which employs Theodorsen theory¹⁰ for calibration. In contrast, the present model is calibrated using data from high-fidelity Euler CFD simulations of the transonic unsteady flow around airfoils. Section II of this paper develops the physics-based low-order model. Section III describes the state-space system identification methods used to fit the model coefficients using CFD data. Section IV demonstrates the model’s ability to predict transonic flutter, and Section V concludes the paper.

II. Physics-Based State-Space Model Formulation

This section develops the physics-based low-order model. We start with the aerodynamic low-order model, of which some coefficients will have to be calibrated—the calibration is discussed in Section III—and then move on to the structural model. The aerodynamic and structural models are combined in an aeroelastic state-space system. Analysis of the coupled state-space system indicates whether flutter occurs.

II.A. Aerodynamic Low-Order Model

The physics-based low-order aerodynamic model begins with the Helmholtz decomposition, which expresses any instantaneous velocity field \mathbf{V} as integrals over the velocity’s divergence and curl fields, commonly known as the volume-source density σ and the vorticity $\boldsymbol{\omega}$:

$$\sigma \equiv \nabla \cdot \mathbf{V} \tag{1}$$

$$\boldsymbol{\omega} \equiv \nabla \times \mathbf{V} \tag{2}$$

$$\mathbf{V}(\mathbf{r}, t) = \frac{1}{2\pi} \iint \sigma(\mathbf{r}', t) \frac{\mathbf{r} - \mathbf{r}'}{|\mathbf{r} - \mathbf{r}'|^2} d\mathcal{A}' + \frac{1}{2\pi} \iint \boldsymbol{\omega}(\mathbf{r}', t) \times \frac{\mathbf{r} - \mathbf{r}'}{|\mathbf{r} - \mathbf{r}'|^2} d\mathcal{A}' + \mathbf{V}_\infty, \tag{3}$$

where \mathbf{r} is a position vector, t is time, and \mathbf{V}_∞ is the free-stream velocity field. For low-speed flow we have $\sigma = 0$ by mass continuity, and for potential flow the $\boldsymbol{\omega}$ field is restricted to the body boundary layers and wakes where it can be approximated via vortex filaments or the equivalent normal-doublet panels. This is the basis of vortex-lattice or doublet-lattice methods. For compressible flows the volume-source field σ becomes significant due to density gradients, but for small-disturbance subsonic flows it can be linearized and removed via the Prandtl-Glauert transformation.³⁶ Although this linearization approach fails for transonic flows, the velocity decomposition (3) is a mathematical identity and always remains valid, provided the volume-source field σ is defined and computed appropriately. One example is given by Oskam,³⁷ who obtained 2D transonic airfoil solutions using this approach. Specifically, the volume-source field was represented by panels covering space around the airfoil, whose σ strengths were computed via the full-potential equation, together with the usual normal-doublet panels on the surface computed via flow tangency.

We define the unsteady volume-source and vorticity fields to have the form

$$\sigma(\mathbf{r}, t) = \sigma_0(\mathbf{r}) + \Delta\sigma(\mathbf{r}, t) \tag{4}$$

$$\boldsymbol{\omega}(\mathbf{r}, t) = \boldsymbol{\omega}_0(\mathbf{r}) + \Delta\boldsymbol{\omega}(\mathbf{r}, t), \tag{5}$$

where σ_0 and $\boldsymbol{\omega}_0$ correspond to some known steady transonic flow, and $\Delta\sigma$ and $\Delta\boldsymbol{\omega}$ are small perturbations defining the unsteady flow we are seeking. Since the Helmholtz decomposition (3) is linear in σ and $\boldsymbol{\omega}$, the corresponding velocity field will have the same baseline plus perturbation form:

$$\mathbf{V}(\mathbf{r}, t) = \mathbf{V}_0(\mathbf{r}) + \Delta\mathbf{V}(\mathbf{r}, t). \tag{6}$$

We stress that “small disturbance” here refers to small disturbances from the steady solution, and not small perturbations from the freestream (which is the more common usage).

To construct the low-order model for the overall airfoil lift and pitching moment, we first assume that the effects of the σ and ω fields, diagrammed in Figure 1, can be captured by only their leading spatial moments. The zeroth moment of the vorticity, or equivalently its overall lumped strength, is the airfoil circulation

$$\Gamma \equiv \iint \omega \cdot \hat{\mathbf{y}} \, d\mathcal{A}, \quad (7)$$

where $\hat{\mathbf{y}}$ is the unit vector into the plane. For steady flow, the circulation captures the lift exactly via the Kutta-Joukowski theorem. As sketched in Figure 1, the volume-source field σ is mostly positive over the upper front of the airfoil where the flow accelerates, and mostly negative over the shock and the upper rear where the flow decelerates. Its zeroth moment is comparable to the wave drag, which typically is very small and negligible compared to the lift force:

$$\frac{D_{\text{wave}}}{\rho_\infty V_\infty} \simeq \iint \sigma \, d\mathcal{A} \simeq 0. \quad (8)$$

Consequently, we must consider the first x -moment of the volume-source field, which is its overall lumped x -doublet strength,

$$\kappa_x(t) \equiv \iint -x \sigma \, d\mathcal{A}. \quad (9)$$

In the single-element Weissinger vortex-lattice method,^{38,39} all the vorticity is lumped into a point vortex placed at the airfoil quarter-chord point, and its strength Γ is implicitly determined by requiring the flow-tangency condition $\mathbf{V}_{c.p.} \cdot \hat{\mathbf{n}}_{c.p.} = 0$ at the control point at the airfoil three-quarter chord point. For unsteady flow there will be additional contributions from the shed vorticity that modify $\mathbf{V}_{c.p.}$ and hence $\Gamma(t)$ and the lift, and also from the airfoil motion. This is the approach used in the ASWING formulation,^{34,35} which for low-speed flow closely matches the results of the more exact Theodorsen theory.¹⁰

For the transonic flows considered here, this model is extended by the addition of the lumped x -doublet placed at some location (x_κ, z_κ) . As diagrammed in Figure 1, the doublet adds to the overall velocity at the control point, and thus will affect Γ and the lift. This is the mechanism which is here postulated to capture the compressibility effects on the circulation and the resulting lift and moment.

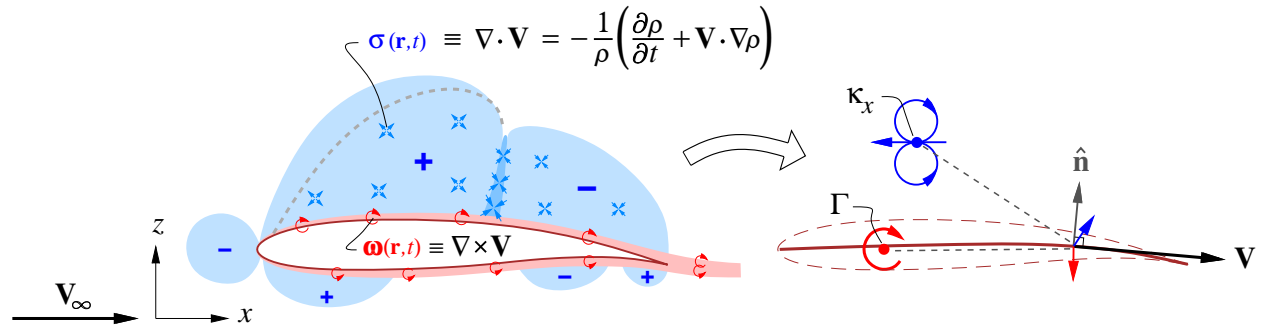


Figure 1. Vorticity and field sources representing velocity field are approximated by overall circulation Γ and doublet κ_x . Only their small unsteady perturbations from a transonic flowfield, $\Delta\Gamma$ and $\Delta\kappa_x$, are sought in the present analysis.

Corresponding to decompositions (4) and (5), we will here actually seek the small perturbations

$$\Delta\Gamma(t) \equiv \Gamma(t) - \Gamma_0 \quad (10)$$

$$\Delta\kappa_x(t) \equiv \kappa_x(t) - \kappa_{x,0} \quad (11)$$

from the steady-solution values $\Gamma_0, \kappa_{x,0}$. The steady circulation Γ_0 is directly proportional to the steady lift coefficient c_{ℓ_0} or the corresponding angle of attack α_0 , while $\kappa_{x,0}$ is also a strong function of the freestream Mach number M_∞ and to some extent of the airfoil shape. Typical $\kappa_{x,0}$ variation for a transonic airfoil is shown in Figure 2. Note that the dependence on c_{ℓ_0} is almost linear.

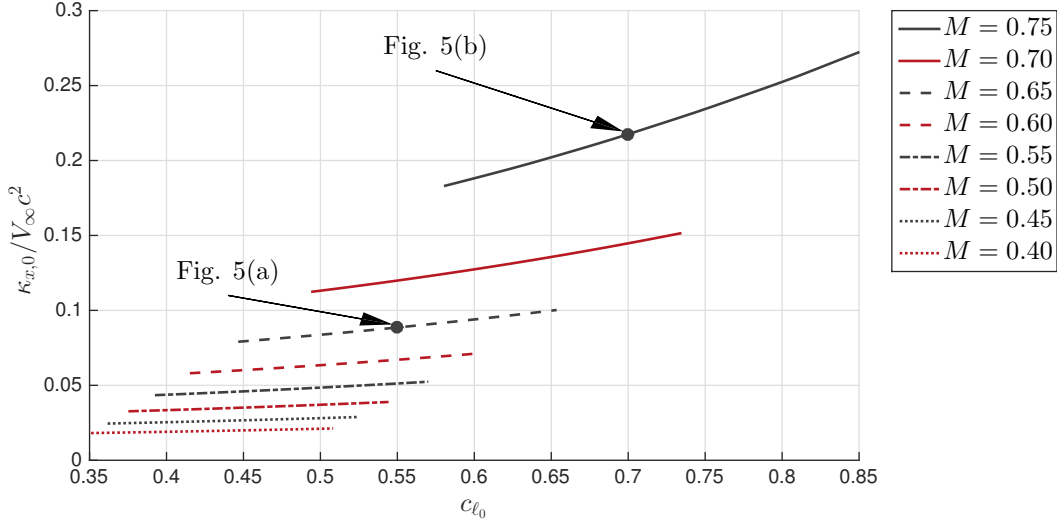


Figure 2. Variation of $\kappa_{x,0}$ with $c_{\ell,0}$ and Mach number for the RAE2822 transonic airfoil, as computed using MSES.^{40–42}

For the imposition of flow tangency at the control point, we define the instantaneous airfoil-surface normal velocity at the control point as

$$U_n(t) \equiv \mathbf{U}_{c.p.} \cdot \hat{\mathbf{n}}_{c.p.}, \quad (12)$$

while the instantaneous fluid normal velocity at the control point is defined as

$$V_n(t) \equiv \mathbf{V}_{c.p.} \cdot \hat{\mathbf{n}}_{c.p.}. \quad (13)$$

Next, we approximate the normal fluid velocity perturbation at the three-quarter control point as

$$\Delta V_n(t) = A_\Gamma \Delta \Gamma + A_{\dot{\Gamma}} \Delta \dot{\Gamma} + A_\kappa \Delta \kappa_x, \quad (14)$$

which can be considered to be a lumped form of the velocity decomposition (3), with the $\Delta \dot{\Gamma}$ term capturing the contribution of the shed vorticity. Following the single-element Weissinger vortex lattice method^{38,39} we set

$$A_\Gamma = -\frac{1}{\pi} \frac{1}{c}, \quad (15)$$

and following the ASWING shed-vorticity model^{34,35} we set

$$A_{\dot{\Gamma}} = -\frac{b}{V_\infty}. \quad (16)$$

The calibrated lag constant value $b = 2/\pi$ gives results that closely approximate those of Theodorsen.¹⁰ If we place the x -doublet at $(x_\kappa, z_\kappa) = (c/2, c/4)$, then the doublet's influence on the three quarter-chord control point gives

$$A_\kappa = \frac{1}{4\pi} \frac{1}{c^2}. \quad (17)$$

In general, however, the effective doublet position is not known, and is expected to depend on the baseline steady solution. Hence, the A_κ coefficient will be a calibrated function of the baseline steady flow solution. Regardless, we obtain the evolution equation for the circulation by requiring flow tangency at the control point,

$$\Delta V_n = U_n \quad (18)$$

$$\Rightarrow A_{\dot{\Gamma}} \Delta \dot{\Gamma} = U_n - A_\Gamma \Delta \Gamma - A_\kappa \Delta \kappa_x. \quad (19)$$

The evolution equation for the x -doublet is postulated to be second-order. This follows from the full potential equation,⁴³

$$\nabla^2 \phi - \frac{1}{a^2} \left[\frac{\partial^2 \phi}{\partial t^2} + \frac{\partial}{\partial t} \left(\frac{\|\mathbf{V}\|^2}{2} \right) + \mathbf{V} \cdot \nabla \left(\frac{\|\mathbf{V}\|^2}{2} \right) \right] = 0. \quad (20)$$

Note that $\nabla^2 \phi = \sigma$, so that taking the Laplacian of Eq. (20) would give a wave equation for σ , involving second time derivatives. Hence, κ_x —the first moment of σ —must at a minimum have a second time derivative in its evolution equation. Therefore, we postulate the evolution equation for κ_x to be

$$\Delta \ddot{\kappa}_x = B_\Gamma \Delta \Gamma + B_\kappa \Delta \kappa_x + B_{\dot{\kappa}} \Delta \dot{\kappa}_x, \quad (21a)$$

where

$$B_\Gamma = B_\Gamma(M_\infty, c_{\ell_0}) \quad (21b)$$

$$B_\kappa = B_\kappa(M_\infty, c_{\ell_0}) \quad (21c)$$

$$B_{\dot{\kappa}} = B_{\dot{\kappa}}(M_\infty, c_{\ell_0}) \quad (21d)$$

are calibrated functions for the airfoil (or airfoil family) being analyzed, and

$$c_{\ell_0} = \frac{2\Gamma_0}{cV_\infty} \quad (22)$$

is the lift coefficient of the baseline solution. The lift and the moment around the elastic axis, per unit span, are

$$\Delta L_c(t) = \rho_\infty V_\infty \Delta \Gamma + \rho_\infty c \Delta \dot{\Gamma} \quad (23a)$$

$$\Delta L(t) = \Delta L_c(t) + \Delta L_{nc}(t) \quad (23b)$$

$$\Delta M(t) = \Delta M_{c/4}(t) + \Delta L_c(t) d + \Delta M_{nc}(t), \quad (23c)$$

where $\Delta M_{c/4}(t) \equiv \frac{1}{2} \rho_\infty V_\infty^2 c^2 \Delta c_m$. Here, Δc_m is a calibrated function of $\Delta \Gamma/cV_\infty$, $\Delta \dot{\Gamma}/V_\infty^2$, $\Delta \kappa_x/c^2 V_\infty$, and $\Delta \dot{\kappa}_x/cV_\infty^2$, using a least-squares fit to a number of unsteady Euler or RANS calculations. Following Theodorsen,¹⁰ the non-circulatory lift $\Delta L_{nc}(t)$ and moment around the elastic axis $\Delta M_{nc}(t)$ are added-mass terms defined as

$$\Delta L_{nc}(t) = \frac{1}{4} \rho_\infty \pi c^2 \left[\Delta \ddot{h} - \left(x_{ea} - \frac{c}{2} \right) \Delta \ddot{\theta} \right] + \frac{1}{4} \rho_\infty \pi c^2 V_\infty \Delta \dot{\theta} \quad (24a)$$

$$\Delta M_{nc}(t) = \frac{1}{4} \rho_\infty \pi c^2 \left(x_{ea} - \frac{c}{2} \right) \left[\Delta \ddot{h} - \left(x_{ea} - \frac{c}{2} \right) \Delta \ddot{\theta} \right] - \frac{\rho_\infty \pi c^4}{128} \Delta \ddot{\theta} - \frac{1}{4} \rho_\infty \pi c^2 V_\infty \left(\frac{3}{4} c - x_{ea} \right) \Delta \dot{\theta}. \quad (24b)$$

II.B. Typical-Section Structural Model

We focus here on *the typical section* (Fig. 3), as used frequently in the aeroelasticity community. Using Hamilton's equation and Lagrangian mechanics, the equations of motion of an airfoil in heave and pitch motion are found to be^{44,45}

$$m \Delta \ddot{h} + k_h \Delta h + S_\theta \Delta \ddot{\theta} = -\Delta L \quad (25a)$$

$$S_\theta \Delta \ddot{h} + k_\theta \Delta \theta + I_\theta \Delta \ddot{\theta} = \Delta M \quad (25b)$$

where here we define Δh to be the heave perturbation, defined positive downward, and $\Delta \theta$ to be the pitch angle perturbation, defined positive clockwise. m is the total mass/span of the section, $S_\theta \equiv (x_{cg} - x_{ea}) m$ is the mass unbalance/span, where x_{cg} and x_{ea} are the distances of the center of gravity and elastic center, respectively, from the leading edge. I_θ is the moment of inertia/span around the elastic axis. Finally, k_h is the heave displacement spring constant/span, and k_θ is the torsional spring constant/span. The pitching moment equation (25b) is constructed about the elastic axis (or shear center) location, defined to be a distance d from the quarter chord point.

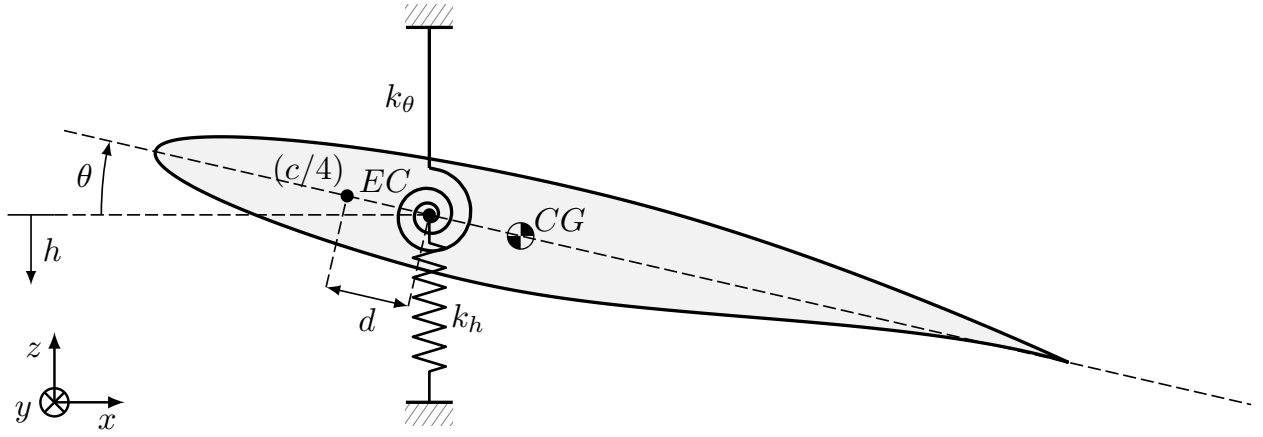


Figure 3. Typical section.

II.C. Overall State Space Model and Flutter Prediction

The aeroelastic model couples the aerodynamic and structural models, using the following overall state vector:

$$\mathbf{x}(t) = [\Delta h(t), \Delta \theta(t), \Delta w(t), \Delta \omega(t), \Delta \Gamma(t), \Delta \kappa_x(t), \Delta \dot{\kappa}_x(t)]^\top, \quad (26)$$

where $\Delta \omega(t) \equiv \Delta \dot{\theta}(t)$ is the pitch rate perturbation and $\Delta w(t) \equiv \Delta \dot{h}(t)$ is the vertical (downward) velocity perturbation. The vertical velocity and pitch rate force the aerodynamic system through the normal velocity at the control point,

$$U_n = \Delta w + V_\infty \Delta \theta + \frac{c}{4} \Delta \omega. \quad (27)$$

The aeroelastic system equations now become

$$\Delta \dot{h} = \Delta w \quad (28a)$$

$$\Delta \dot{\theta} = \Delta \omega \quad (28b)$$

$$\begin{aligned} m \Delta \dot{w} + S_\theta \Delta \dot{\omega} &= -k_h \Delta h - \Delta L \\ &= -k_h \Delta h - \rho_\infty V_\infty \Delta \Gamma - \rho_\infty c \Delta \dot{\Gamma} \\ &= -k_h \Delta h - \rho_\infty V_\infty \Delta \Gamma \\ &\quad - \frac{\rho_\infty c}{A_\Gamma} \left(\Delta w + V_\infty \Delta \theta + \frac{c}{4} \Delta \omega - A_\Gamma \Delta \Gamma - A_\kappa \Delta \kappa_x \right) - \Delta L_{nc}(t) \end{aligned} \quad (28c)$$

$$\begin{aligned} S_\theta \Delta \dot{w} + I_\theta \Delta \dot{\omega} &= -k_\theta \Delta \theta + \Delta L d + \Delta M \\ &= -k_\theta \Delta \theta + \rho_\infty V_\infty \Delta \Gamma d + \frac{\rho_\infty c}{A_\Gamma} \left(\Delta w + V_\infty \Delta \theta + \frac{c}{4} \Delta \omega - A_\Gamma \Delta \Gamma - A_\kappa \Delta \kappa_x \right) d \\ &\quad + \Delta M_{c/4} + \Delta M_{nc}(t) \end{aligned} \quad (28d)$$

$$\Delta \dot{\Gamma} = \frac{1}{A_\Gamma} \left[\Delta w + V_\infty \Delta \theta + \frac{c}{4} \Delta \omega - A_\Gamma \Delta \Gamma - A_\kappa \Delta \kappa_x \right] \quad (28e)$$

$$\Delta \dot{\kappa}_x = B_\Gamma \Delta \Gamma + B_\kappa \Delta \kappa_x + B_{\dot{\kappa}} \Delta \dot{\kappa}_x. \quad (28f)$$

Eq. (28) has the form of a standard descriptor state-space model

$$\mathbf{E} \dot{\mathbf{x}} = \mathbf{A} \mathbf{x}. \quad (29)$$

Flutter is indicated if any eigenvalue of the matrix $(\mathbf{E}^{-1} \mathbf{A})$ has a positive real part. The unknown coefficients of the \mathbf{E} , \mathbf{A} matrices are calibrated using CFD simulations of forced pitching and heaving airfoil motions, as described in the next section.

III. Model Fitting from CFD Data

This section describes our approach to fit the unknown coefficients of the low-order flutter model using data generated with unsteady CFD simulations. The structural dynamics of the typical-section airfoil are the same for subsonic and transonic flows, and it is only the aerodynamic model that needs calibration for transonic flows. Therefore, we decompose the state-space system in Eq. (29), to extract the aerodynamic state-space system with state \mathbf{x}_a , input \mathbf{u}_a , and state-space matrices \mathbf{A}_a and \mathbf{B}_a , defined as follows:

$$\frac{d}{dt} \begin{bmatrix} \Delta\Gamma(t) \\ \Delta\kappa_x(t) \\ \Delta\dot{\kappa}_x(t) \end{bmatrix} = \underbrace{\begin{bmatrix} -\frac{A_\Gamma}{A_\Gamma} & -\frac{A_\kappa}{A_\Gamma} & 0 \\ 0 & 0 & 1 \\ B_\Gamma & B_\kappa & B_{\dot{\kappa}} \end{bmatrix}}_{\mathbf{A}_a} \underbrace{\begin{bmatrix} \Delta\Gamma(t) \\ \Delta\kappa_x(t) \\ \Delta\dot{\kappa}_x(t) \end{bmatrix}}_{\mathbf{x}_a} + \underbrace{\begin{bmatrix} \frac{V_\infty}{A_\Gamma} & \frac{c/4}{A_\Gamma} & \frac{1}{A_\Gamma} \\ 0 & 0 & 0 \\ 0 & 0 & 0 \end{bmatrix}}_{\mathbf{B}_a} \underbrace{\begin{bmatrix} \Delta\theta(t) \\ \Delta\omega(t) \\ \Delta w(t) \end{bmatrix}}_{\mathbf{u}_a} \quad (30)$$

III.A. State-space System Identification

The unknown coefficients in the low-order flutter model developed in Section II are A_Γ , A_κ , B_Γ , B_κ , $B_{\dot{\kappa}}$. To determine these coefficients from data, we employ the state-space system identification method of Dynamic Mode Decomposition (DMD).⁴⁶ Specifically, we use dynamic mode decomposition with control (DMDc),⁴⁷ which requires us to collect snapshots of the states and control inputs at each time step. Therefore, we first run unsteady compressible flow simulations for forced pitching/heaving oscillations to obtain $\{\Delta\Gamma(t_i), \Delta\kappa_x(t_i), \Delta\theta(t_i), \Delta\omega(t_i), \Delta w(t_i)\}$ with $t_i = (i-1)\Delta t$, $i = 1, \dots, (N+2)$.

These snapshots are collected in the matrices $X \in \mathbb{R}^{1 \times N}$, $X' \in \mathbb{R}^{2 \times N}$, $X'' \in \mathbb{R}^{2 \times N}$, and $\Upsilon' \in \mathbb{R}^{3 \times N}$ as follows:

$$X = \begin{bmatrix} \Delta\kappa_x(t_1) & \Delta\kappa_x(t_2) & \dots & \Delta\kappa_x(t_N) \end{bmatrix}, \quad (31a)$$

$$X' = \begin{bmatrix} \Delta\Gamma(t_2) & \Delta\Gamma(t_3) & \dots & \Delta\Gamma(t_{N+1}) \\ \Delta\kappa_x(t_2) & \Delta\kappa_x(t_3) & \dots & \Delta\kappa_x(t_{N+1}) \end{bmatrix}, \quad (31b)$$

$$X'' = \begin{bmatrix} \Delta\Gamma(t_3) & \Delta\Gamma(t_4) & \dots & \Delta\Gamma(t_{N+2}) \\ \Delta\kappa_x(t_3) & \Delta\kappa_x(t_4) & \dots & \Delta\kappa_x(t_{N+2}) \end{bmatrix}, \quad (31c)$$

$$\Upsilon' = \begin{bmatrix} \Delta\theta(t_2) & \Delta\theta(t_3) & \dots & \Delta\theta(t_{N+1}) \\ \Delta\omega(t_2) & \Delta\omega(t_3) & \dots & \Delta\omega(t_{N+1}) \\ \Delta w(t_2) & \Delta w(t_3) & \dots & \Delta w(t_{N+1}) \end{bmatrix}. \quad (31d)$$

Note that we need the matrix X'' because we postulated the evolution equation for κ_x to be second-order in Eq. (21a).

DMD fits a discrete state-space system, relating X'' to X' , X and Υ' as

$$X'' \approx aX' + a_l X + b\Upsilon', \quad (32)$$

where $a \in \mathbb{R}^{2 \times 2}$, $a_l \in \mathbb{R}^{2 \times 1}$, $b \in \mathbb{R}^{2 \times 3}$ are matrices containing the unknown coefficients to be fit. Eq. (32) can be rewritten in the form

$$X'' \approx G\Omega, \quad (33)$$

with $G = \begin{bmatrix} a & a_l & b \end{bmatrix} \in \mathbb{R}^{2 \times 6}$ and $\Omega = \begin{bmatrix} X' \\ X \\ \Upsilon' \end{bmatrix} \in \mathbb{R}^{6 \times N}$.

In Eq. (33), X'' and Ω are obtained from the CFD simulations, and G is then found by solving the least-squares optimization problem

$$G = \arg \min_G \|X'' - G\Omega\|_F. \quad (34)$$

To solve this minimization problem, one computes a singular value decomposition (SVD) of $\Omega = U\Sigma V^\top$, where $U \in \mathbb{R}^{6 \times 6}$, $V \in \mathbb{R}^{N \times 6}$, and the diagonal matrix $\Sigma \in \mathbb{R}^{6 \times 6}$. The least-squares fit G is then found to be

$$G = X''V\Sigma^{-1}U^\top. \quad (35)$$

In contrast to the reduced-order modeling approach where DMD is typically used, we do not truncate the singular values in Σ when computing G . In reduced-order modeling, the row dimension of the snapshot matrices is the total number of states in the CFD model (typically 10^4 or higher), and DMD is used to identify a model of much lower order. In contrast, in this system identification setting, we construct the data matrices X , X' , X'' , and Y' with our six physical low-order quantities, such that the state dimension of the DMD representation is already at the desired number.

The matrices a , a_l , and b are found by decomposing the linear operator U as

$$\begin{bmatrix} a, & a_l, & b \end{bmatrix} \approx \begin{bmatrix} X''V\Sigma^{-1}U_1^\top, & X''V\Sigma^{-1}U_2^\top, & X''V\Sigma^{-1}U_3^\top \end{bmatrix}, \quad (36)$$

where $U_1 \in \mathbb{R}^{6 \times 2}$, $U_2 \in \mathbb{R}^{6 \times 1}$, $U_3 \in \mathbb{R}^{6 \times 3}$ are the first two columns of U , the third column of U , and the last three columns of U .

Finally, we relate the discrete state-space matrices a , a_l , b to the continuous state-space matrices A_a and B_a in Eq. (30) using Tustin's method.⁴⁸

The process described in this section allows for fitting one state space model for one particular freestream Mach number, airfoil and baseline lift coefficient. We would like to characterize the flutter boundary for a range of Mach numbers, airfoil thicknesses, and baseline lift coefficients. Therefore, the method described in this section is used to find the aerodynamic state space matrices for a set of freestream Mach numbers, baseline lift coefficients, and different thicknesses of the same airfoil family. Splines are then fit for the entries in the aerodynamic state space matrices to find a low-order model at an interpolatory Mach number, baseline lift coefficient, and/or airfoil thickness.

III.B. CFD Data Generation

We fit the aerodynamic part of the state-space system using data from CFD solutions. Throughout this work, we use the SU2 tool suite.⁴⁹ SU2 is a multi-purpose PDE solver, and specifically developed with aerospace applications in mind, such as unsteady compressible flow over an airfoil. For CFD applications, SU2 employs a finite volume method with standard edge-based structure on a dual grid. For unsteady simulations it uses a dual time-stepping strategy for high-order accuracy in time.⁵⁰

Two changes to SU2 were necessary for this work. First, the parameters of our problem (κ_x , Γ) are computed by post-processing SU2 solutions. The circulation $\Gamma(t)$ is defined as

$$\Gamma(t) \equiv \iint \boldsymbol{\omega}(t) \cdot \hat{\mathbf{y}} \, d\mathcal{A} = \oint \mathbf{V}(t) \cdot d\mathbf{l}. \quad (37)$$

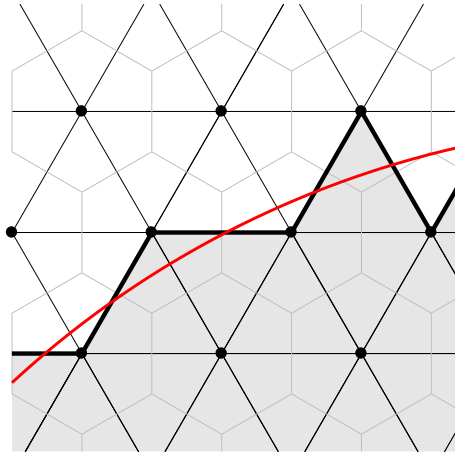
If this line integral is computed sufficiently close to the airfoil, it is more accurate than integrating the vorticity, because this is less susceptible to round-off errors and noise in the gradient computation. Note that we need to choose the contour for the line integral to exclude the wake, such that we compute the circulation *without* including shed vorticity. This is illustrated in Fig. 4(c).

Computing the x -doublet through integration of the divergence of the velocity field is even more problematic, because the extrema in the volume-source field are highly localized. As an example, the volume-source field around the RAE2822 airfoil in subsonic and transonic flow is shown in Fig. 5 for different lift coefficients, as computed with MSES.⁴⁰⁻⁴² Using the contour shown in Fig. 4(b), the x -doublet is computed by evaluating

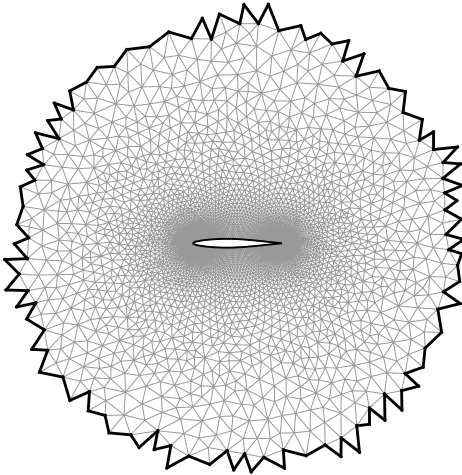
$$\begin{aligned} \kappa_x(t) &= - \iint x \nabla \cdot \mathbf{V}(t) \, d\mathcal{A} = - \oint x \mathbf{V}(t) \cdot \hat{\mathbf{n}} \, ds + \iint U(t) \, d\mathcal{A} \\ &= - \oint x [\mathbf{V}(t) - \mathbf{V}_\infty] \cdot \hat{\mathbf{n}} \, ds + \iint [U(t) - U_\infty] \, d\mathcal{A}, \end{aligned} \quad (38)$$

where U is the velocity in the freestream x -direction. The final expression for $\kappa_x(t)$ subtracts off \mathbf{V}_∞ to minimize cancellation errors.

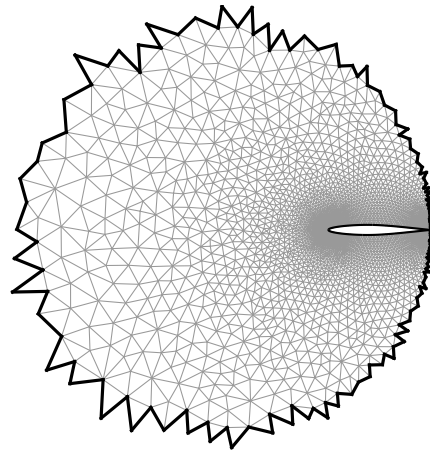
When using a structured grid (e.g., an O-grid or a C-grid for airfoils), computing these quantities using line integrals is straightforward. One can just track the grid lines at a certain distance around the airfoil. However, throughout this work we mostly used unstructured grids, complicating the computation of the line integrals. In this case, we find a set of edges in the mesh at a certain distance from the airfoil that form a closed loop around that airfoil. First, the set of edges that intersect a circle centered around the airfoil is identified, by finding the edges for which one edge point is inside the circle and one is outside on the



(a) Detail of triangular mesh with cut. Black lines indicate primal grid with nodes (circles), thick black lines indicate the line along which the line integrals are computed.



(b) Mesh of NACA64A010 airfoil with line around airfoil that is used for the line integral in the computation of the x -doublet κ_x .



(c) Mesh of NACA64A010 airfoil with line around airfoil that is used for the line integral in the computation of the circulation Γ .

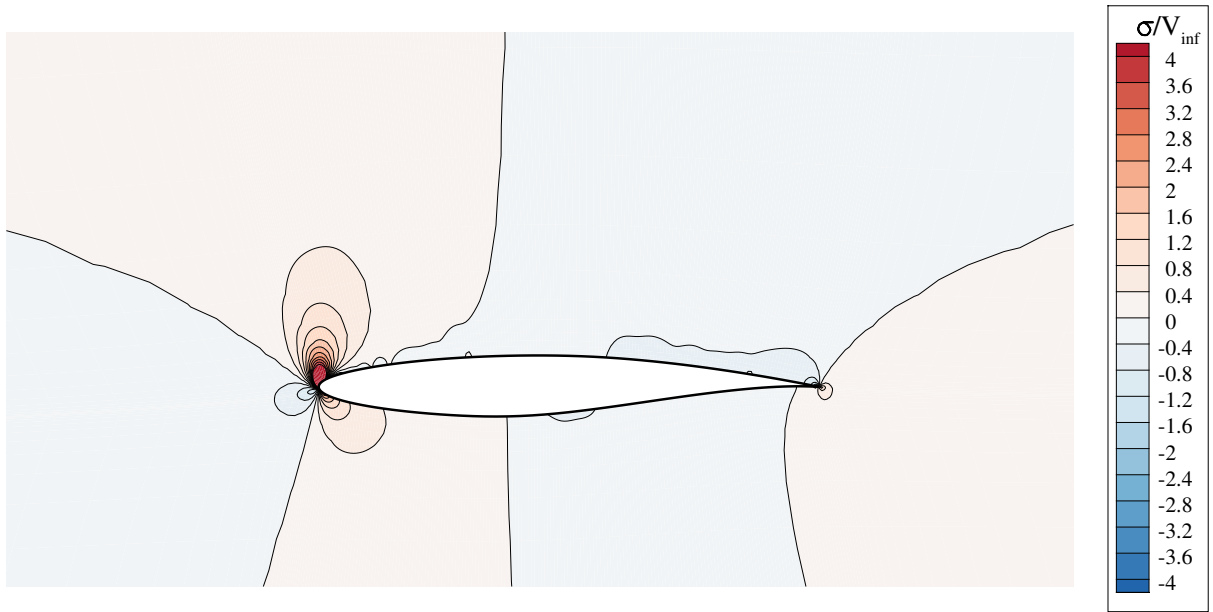
Figure 4. Details of meshes to illustrate how the circulation and x -doublet are computed through line integrals.

circle (see Fig. 4(a)). An arbitrary precision method by Shewchuk⁵¹ is employed for this. Subsequently any hanging nodes are removed from this set. The result of such an approach is shown in Fig. 4(b). For the doublet computation, we must also integrate the U velocity within this circle, which is done by summing over all cells of the primal grid (instead of the dual grid, which SU2 uses).

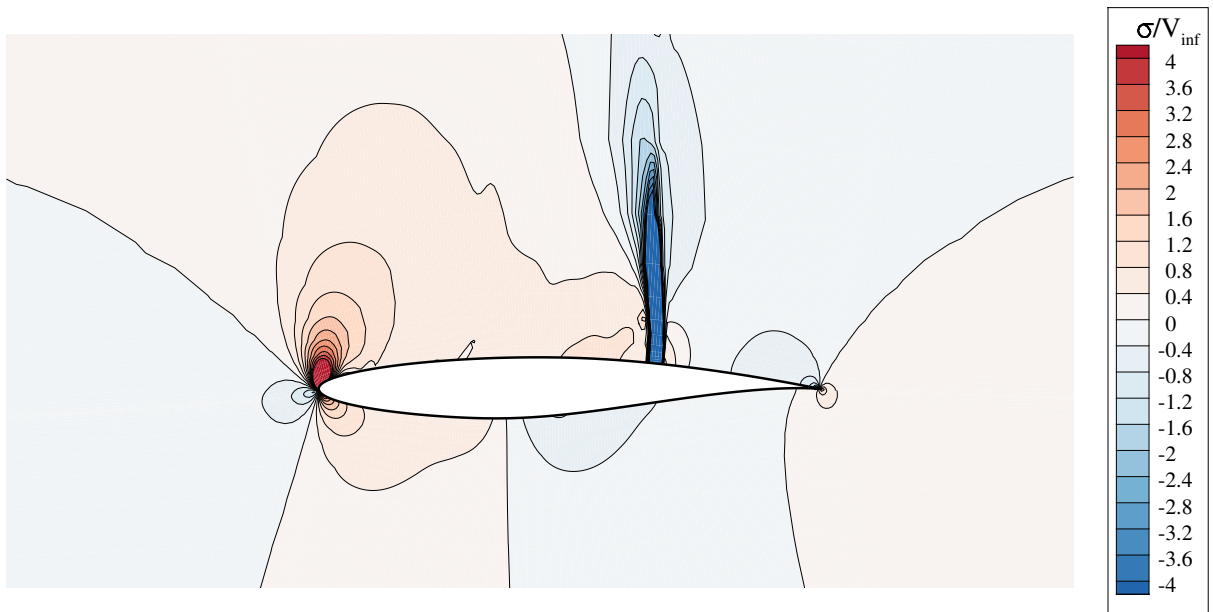
The second change to SU2 was to alter the dynamic mesh rotations in order to allow for different prescribed motions (which include multiple frequencies with a ramp-up to maximum amplitude) and to allow for restarting the solution from a steady result without any discontinuities in the grid velocities. An example of such a prescribed motion is shown in Fig. 6.

IV. Results

Using the methodology outlined in Sections II and III, low-order models are constructed for several different airfoils. Using these low-order models, we investigate the influence of airfoil shape, baseline lift



(a) Subsonic flow, $M_\infty = 0.65$, $c_\ell = 0.55$ ($M_{crit} = 0.699$)



(b) Transonic flow, $M_\infty = 0.75$, $c_\ell = 0.70$ ($M_{crit} = 0.535$)

Figure 5. Volume-source fields around RAE2822 airfoil in subsonic and transonic flow as computed by MSES.^{40–42}

coefficient and Mach number on the transonic flutter boundary. The accuracy of the low-order model is also validated for the standard Isogai Case A.

IV.A. Example Calibration Results for RAE2822 Airfoil

The low-order model is calibrated using Euler simulations of pitching and heaving airfoils at different Mach numbers and reduced frequencies. The results in this section use simulations of an RAE2822 transonic airfoil in forced pitching motion along the path shown in Fig. 6 with an amplitude of $\theta = 0.3^\circ$, and also in a forced

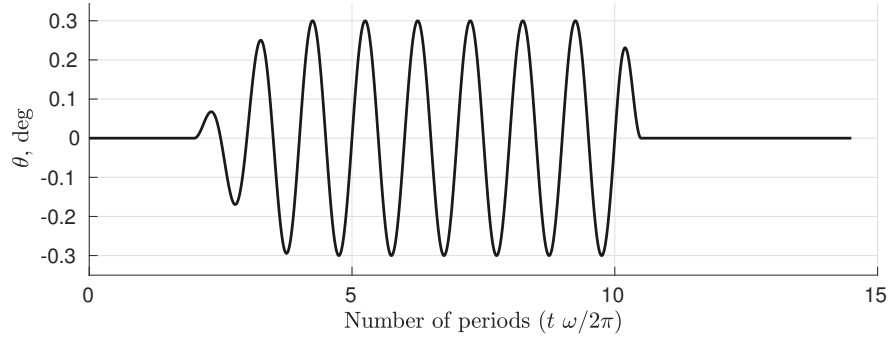


Figure 6. Example of forced pitching oscillation.

heaving motion using a similar trajectory for \dot{h} with an amplitude of $\dot{h}/V_\infty = 0.005$.

First, we show the results of just the SU2 forced-heaving simulations for different Mach numbers in Figures 7 and 8. Both the phase and the magnitude variation of the circulation and the x -doublet are seen to significantly depend on the forcing reduced frequency $\bar{\omega}$, and its effect varies with the baseline Mach number M_∞ . At the higher transonic Mach number, the dependence of the x -doublet phase on frequency is especially strong. A physical explanation of this behavior is that the delays in propagation of the shock and acoustic waves which comprise the σ field variation will be strongly affected by the size of the supersonic zone, and hence by M_∞ .

These CFD results for different Mach numbers and different reduced frequencies are then used to calibrate a low-order model. In this work, we focus on fitting one low-order model per Mach number for reduced frequencies in the range of $\bar{\omega} = 0.05$ to $\bar{\omega} = 0.40$. In the DMD formulation of Section III, we require that all CFD simulations use the same fixed time step Δt . Therefore, the low frequency simulations use more time steps than the high frequency simulations. Throughout this work, we set the time step such that for the highest reduced frequency 40 time steps per period are used.

For the calibration we combine the forced pitching and heaving simulations to yield one fit per Mach number and airfoil. Applying the DMD method of Section III to these CFD results yields the fits shown in Figures 9 and 10 for pitching motion, and Fig. 11 for heaving motion. The low-order model captures the circulation response quite accurately. Capture of the x -doublet response is quite reasonable as well, except for the final part after we stop forcing the airfoil. This is likely due to the numerical noise in the SU2 computation, which then also throws off the fit.

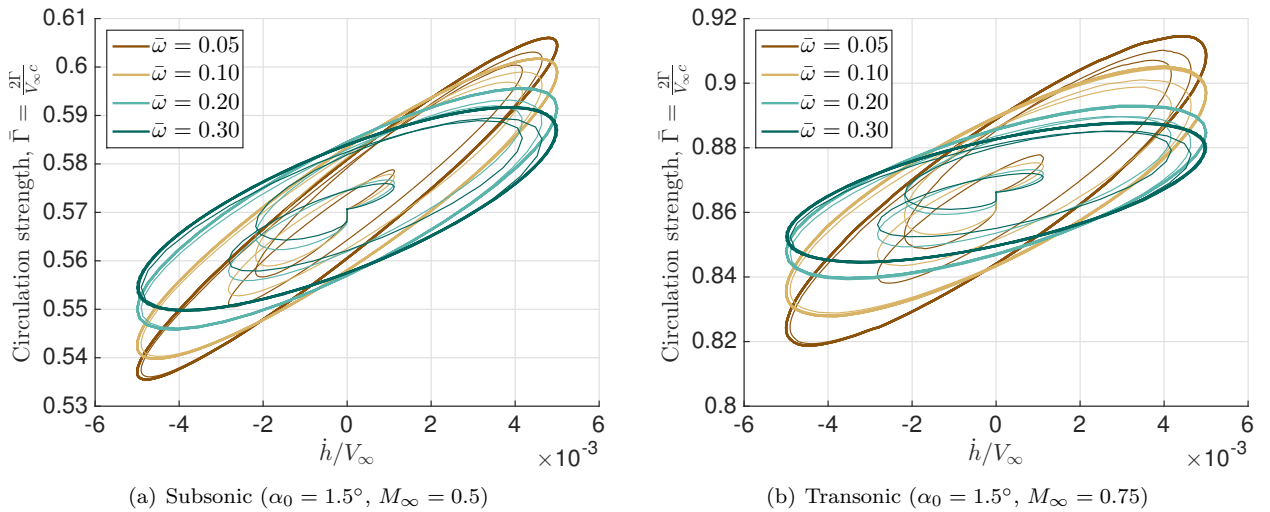


Figure 7. Phase diagram of Γ for forced heaving at different reduced frequencies for subsonic and transonic flow.

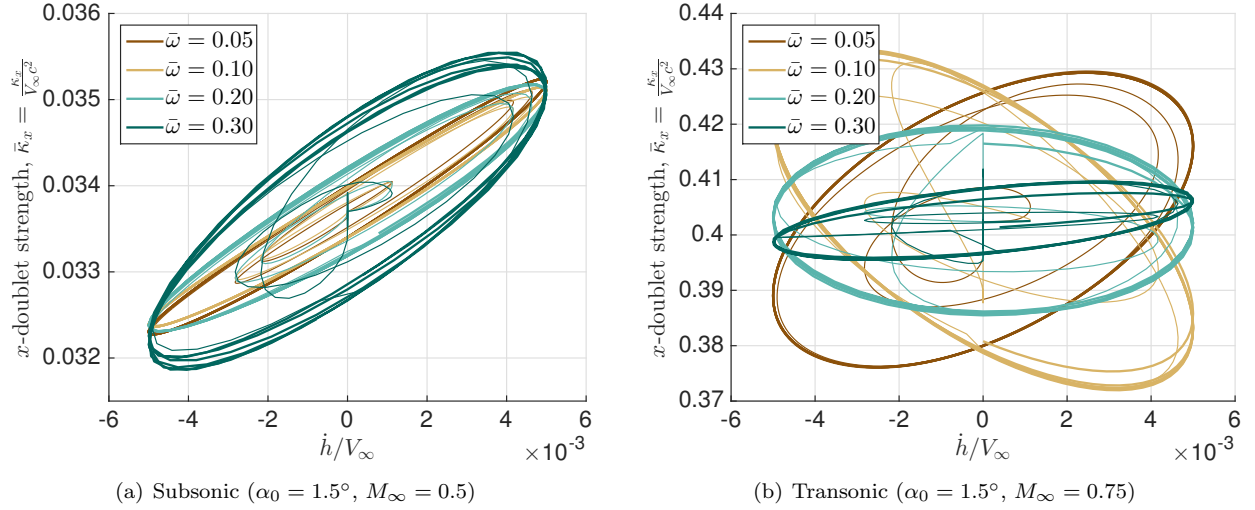


Figure 8. Phase diagram of κ_x for forced heaving at different reduced frequencies for subsonic and transonic flow.

We also show the errors in the fit for different Mach numbers in Tables 1 and 2. The error in each state is computed as

$$\epsilon_i = \frac{\|x_{i,DMD} - x_{i,SU2}\|_2}{\|x_{i,SU2}\|_2}. \quad (39)$$

The results in Tables 1 and 2 confirm that the fit for circulation is significantly better than the fit for the x -doublet.

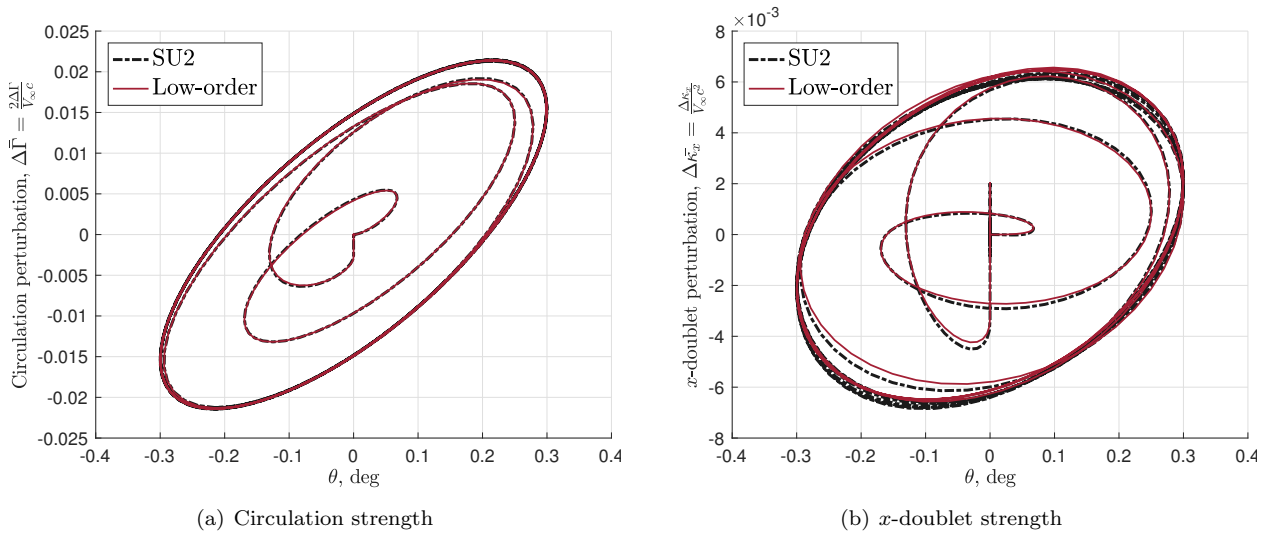


Figure 9. Comparison of phase diagrams between SU2 results and low-order model for forced pitching oscillations at $\bar{\omega} = 0.35$ for $M_\infty = 0.6$ for the RAE2822 airfoil with $\alpha_0 = 1.5^\circ$ ($M_{crit} = 0.648$).

The goal of a calibrated low-order model is to be predictive at different frequencies. We calibrate one low-order model for $M_\infty = 0.30$ and one low-order model for $M_\infty = 0.70$, and test these low-order models at frequencies that were not part of the frequencies used for calibration. Tables 3 and 4 show the accuracy of the DMD fits for these Mach numbers. We see that the accuracy for these frequencies is quite similar to the accuracy for frequencies that were part of the calibration (Tables 1 and 2).

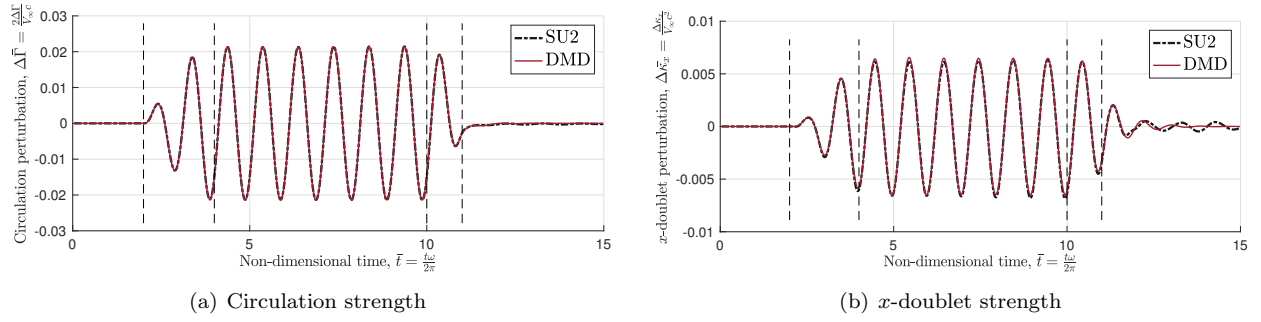


Figure 10. Comparison of time series between SU2 results and low-order model for forced pitching oscillations at $\bar{\omega} = 0.35$ for $M_\infty = 0.6$ for the RAE2822 airfoil with $\alpha_0 = 1.5^\circ$ ($M_{\text{crit}} = 0.648$).

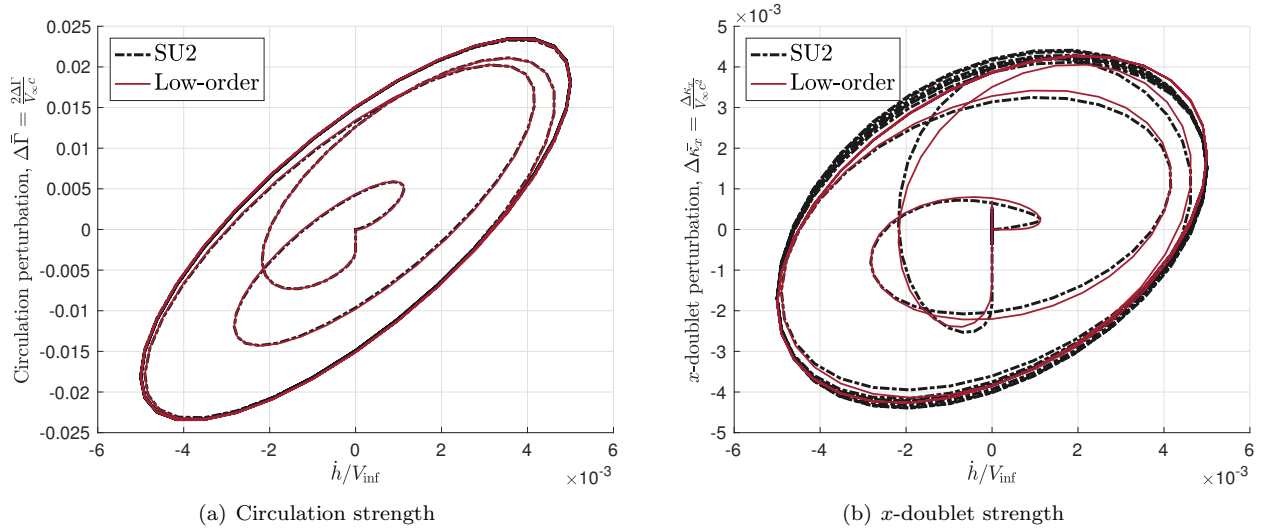


Figure 11. Comparison of phase diagrams between SU2 results and low-order model for forced heaving oscillations at $\bar{\omega} = 0.25$ for $M_\infty = 0.6$ for the RAE2822 airfoil with $\alpha_0 = 1.5^\circ$ ($M_{\text{crit}} = 0.648$).

Table 1. Accuracy of DMD fit for forced pitching oscillations at $M_\infty = 0.30$ for RAE2822 airfoil with $\alpha_0 = 1.5^\circ$ ($M_{\text{crit}} = 0.648$).

$\bar{\omega}$	Error Γ	Error κ_x
0.05	2.8%	7.7%
0.10	2.5%	5.7%
0.15	2.9%	11.5%
0.20	2.7%	16.6%
0.25	2.3%	16.2%
0.30	1.5%	12.1%
0.35	1.3%	13.0%
0.40	3.9%	19.5%

Table 2. Accuracy of DMD fit for forced pitching oscillations at $M_\infty = 0.70$ for RAE2822 airfoil with $\alpha_0 = 1.5^\circ$ ($M_{\text{crit}} = 0.648$).

$\bar{\omega}$	Error Γ	Error κ_x
0.05	4.9%	4.1%
0.10	3.8%	5.9%
0.15	2.5%	14.4%
0.20	2.8%	4.8%
0.25	5.8%	12.4%
0.30	3.6%	16.1%
0.35	1.5%	12.9%
0.40	5.8%	16.3%

We fit low-order models for different freestream Mach numbers to investigate the effect of compressibility

Table 3. Accuracy of DMD fit for forced pitching oscillations at frequencies that were not part of the DMD calibration ($M_\infty = 0.30$ for RAE2822 airfoil with $\alpha_0 = 1.5^\circ$, $M_{\text{crit}} = 0.648$).

$\bar{\omega}$	Error Γ	Error κ_x
0.125	2.7%	8.5%
0.175	2.9%	14.4%
0.225	2.5%	17.1%
0.275	1.9%	14.5%
0.325	1.1%	10.9%
0.375	2.4%	16.7%

Table 4. Accuracy of DMD fit for forced pitching oscillations at frequencies that were not part of the DMD calibration ($M_\infty = 0.70$ for RAE2822 airfoil with $\alpha_0 = 1.5^\circ$, $M_{\text{crit}} = 0.648$).

$\bar{\omega}$	Error Γ	Error κ_x
0.125	3.6%	17.2%
0.175	2.2%	9.7%
0.225	4.9%	6.6%
0.275	4.9%	19.0%
0.325	2.4%	13.2%
0.375	3.4%	9.8%

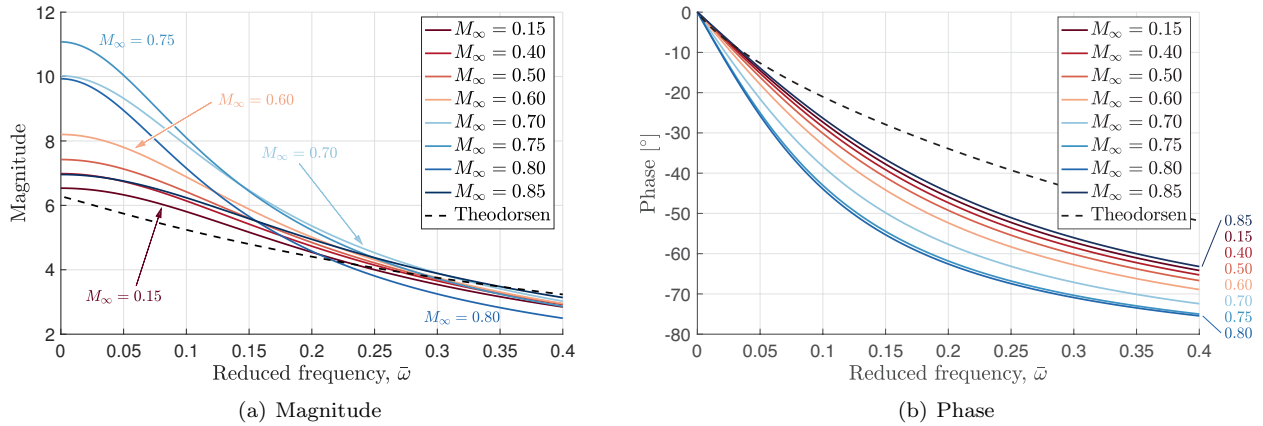


Figure 12. Bode plot of transfer function between non-dimensional circulation ($2\Gamma/V_\infty c$) and pitch angle θ for different Mach numbers for the RAE2822 airfoil with $\alpha_0 = 1.5^\circ$ ($M_{\text{crit}} = 0.648$).

on the aerodynamic response of the airfoil. The effect of Mach number is shown by the magnitude and phase of the transfer function between circulation and the pitching angle θ in Fig. 12, where we also show the result for Theodorsen’s theory. We see that the magnitude of the transfer function is strongly dependent on Mach number, as expected, but that the Mach number influence becomes smaller as the reduced frequency increases. The magnitude of the transfer function is also quite different between subsonic and transonic Mach numbers. Furthermore, the phase lag increases with subsonic Mach number and the Mach number dependence becomes stronger as the reduced frequency increases. For high transonic Mach numbers (e.g., $M_\infty = 0.85$), however, the phase lag suddenly becomes smaller. The trends in these Bode plots are similar to Theodorsen theory, but the values are noticeable different, even for low Mach numbers. This is likely due to considering an airfoil with thickness rather than a flat plate.

This low-order model can be used to investigate the effect of Mach number on the flutter boundary of the RAE2822 airfoil. Low-order models of the form Eq. (30) are fit using DMD at different freestream Mach numbers. For a given Mach number, the aerodynamic low-order model is coupled to the structural model—with airfoil parameters as listed in Table 5—to obtain the full aeroelastic state space model in Eq. (30). Here, we focus on the flutter speed as a function of the center of gravity position. The eigenvalues of $(\mathbf{E}^{-1}\mathbf{A})$ for a given x_{cg} are a function of V_∞ . A bisection method is used to find that flutter speed index V_μ for which the aeroelastic system becomes unstable, the results are shown in Fig. 13. The flutter speed index V_μ is a nondimensionalization of the freestream velocity at which flutter occurs, and is defined as $V_\mu = 2 V_\infty / \sqrt{\mu} \omega_\theta c$. This bisection search is performed *online* and only involves solving 7×7 eigenvalue problems. Constructing one flutter boundary in Fig. 13 for sixty different x_{cg} locations therefore only takes ~ 0.1 s.

Fig. 13 shows that for x_{cg} far forward—or low reduced frequency—a higher subsonic Mach number

lowers the flutter speed. However, as the center of gravity moves aft—at high reduced frequencies—a higher subsonic Mach number increases the flutter speed. The behavior for transonic Mach numbers is quite different, especially for x_{cg} far forward. For instance, for x_{cg} far forward, the flutter speed for $M_\infty = 0.80$ and $M_\infty = 0.85$ is higher than for $M_\infty = 0.70$, which is classic transonic flutter behavior and commonly described as the “transonic dip”.

Airfoil parameter		
RAE2822 ($\alpha_0 = 1.5^\circ$, $M_{crit} = 0.648$)		
Apparent-mass ratio	$\mu = 4m/\pi\rho_\infty c^2$	4.16
Inertia/mass ratio	$r_\theta^2 = 4I_\theta/mc^2$	1.60
Elastic axis position	x_{ea}/c	0.50
In-vacuo heave natural frequency	$\omega_h = \sqrt{k_h/m}$	$\sqrt{50.0}$
In-vacuo pitch natural frequency	$\omega_\theta = \sqrt{k_\theta/I_\theta}$	$\sqrt{400}$

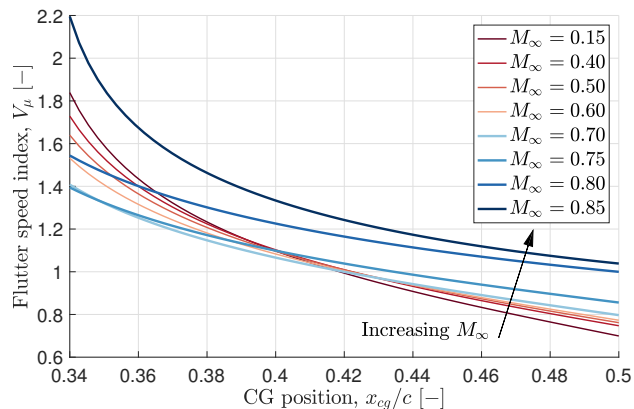


Table 5. Airfoil parameters used for flutter calculations in Fig. 13, from Ref. 52.

Figure 13. Flutter speed versus x_{cg}/c positions for different freestream Mach numbers.

IV.B. Validation — Isogai Case A

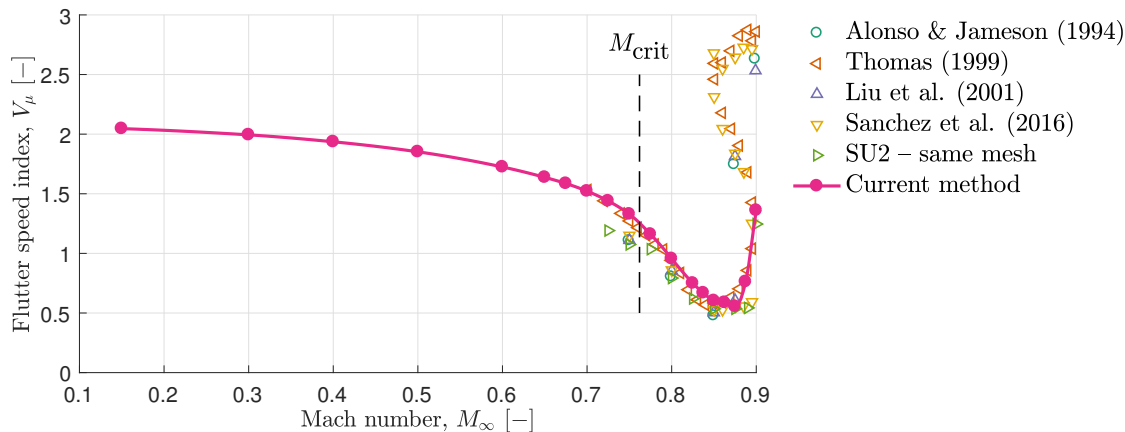


Figure 14. Comparison of transonic flutter boundary for Isogai Case A^{20,53} as found by our method and methods from literature.^{54–57} $M_{crit} = 0.762$ for this case.

We validate the accuracy of the model using the standard Isogai case A.^{20,53} We compare our results for the flutter boundary against four methods from the literature^{54–57} and against the flutter boundary found using SU2 (using the same mesh as was used to calibrate the model). We see that the agreement for the transonic flow regime is quite good up to $M_\infty = 0.9$. Isogai Case A is known for the characteristic S-shape of its flutter boundary. For high transonic Mach numbers, the airfoil becomes unstable but if the flutter speed index is increased further, it becomes stable again, until it finally becomes unstable again around $V_\mu \simeq 2.8$. Our model will be implemented in an aircraft design code to yield flutter predictions of optimal designs. A good design should never operate in the second stability region and therefore it is not a problem that the model cannot capture this S-shape of the flutter boundary.

IV.C. Results Across Airfoil Shape Family

As mentioned before, this model is calibrated as a function of freestream Mach number M_∞ , airfoil family and baseline lift coefficient c_{ℓ_0} . Fig. 15 shows the influence of the baseline lift coefficient and freestream Mach number on the flutter boundary of an 11% transonic airfoil of the C-airfoil family (shown in Fig. 16). Note that the dots in this figure indicate a freestream Mach number where the model was calibrated, whereas the lines in between are generated using splines for the entries in the aerodynamic state space matrix. For low subsonic freestream Mach numbers the dependence of the flutter boundary on baseline lift coefficient is small, however for the transonic regime, the baseline lift coefficient has a larger influence on the transonic flutter boundary. For this airfoil, a lower c_{ℓ_0} is associated with a higher flutter speed index for subsonic Mach numbers, but a lower flutter speed index for high transonic Mach numbers.

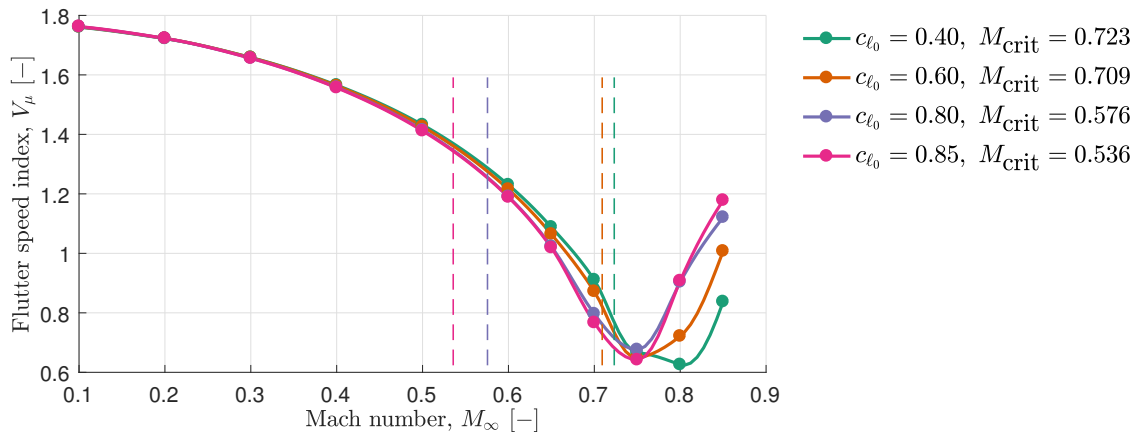


Figure 15. Influence of baseline lift coefficient c_{ℓ_0} on the transonic flutter boundary for the 11% C-airfoil. For this case $\mu = 40$, $\omega_\theta/\omega_h = 0.9$, $r_\theta^2 = 2.5$, $x_{ea}/c = -0.35$, $x_{eg}/c = 0.35$.

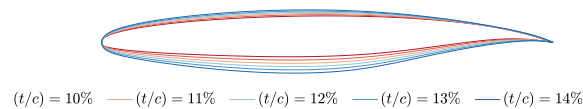


Figure 16. Overview of C-airfoil family.



Figure 17. Comparison between C-airfoil and E-airfoil (12%).

Bendiksen showed that the airfoil thickness can have a large effect on the flutter boundary in the transonic flow and that linear theory predicts that thinner wings would be less susceptible to flutter, but in practice the opposite has been observed in the transonic flow regime.⁴ A flutter boundary for airfoils with different thicknesses of the same airfoil family is shown in Fig. 18. These results indeed confirm that for subsonic freestream Mach numbers, a thicker airfoil is more susceptible to flutter. However, a thinner airfoil is more susceptible to flutter for high transonic freestream Mach numbers.

To highlight the sensitivity of the model to a particular airfoil, we compare the flutter boundary for two different transonic airfoils, which are shown in Fig. 17. These airfoils are quite similar, and Fig. 19 shows that their flutter boundary is almost the same for subsonic Mach numbers. However, for the transonic flow regime their flutter characteristics are quite different, demonstrating that the model is able to pick up on slight differences in airfoil characteristics.

V. Conclusion

This paper highlighted the construction of a physics-based low-order model for unsteady transonic two-dimensional flow over airfoils. The unknown parameters in the model's aerodynamic state-space formulation

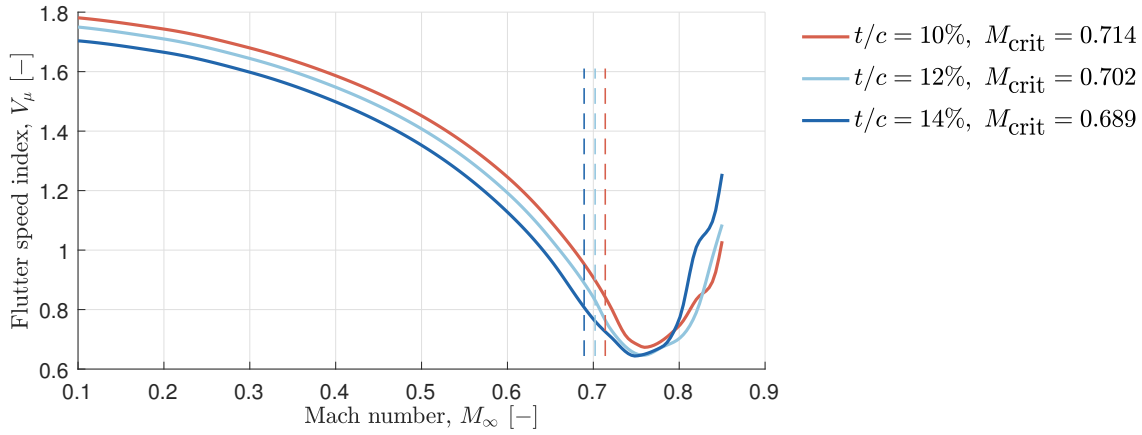


Figure 18. Influence of airfoil thickness on the transonic flutter boundary for the C-airfoil family at $c_{l_0} = 0.6$. For this case $\mu = 40$, $\omega_{\theta}/\omega_h = 0.9$, $r_{\theta}^2 = 2.5$, $x_{ea}/c = -0.35$, $x_{cg}/c = 0.35$.

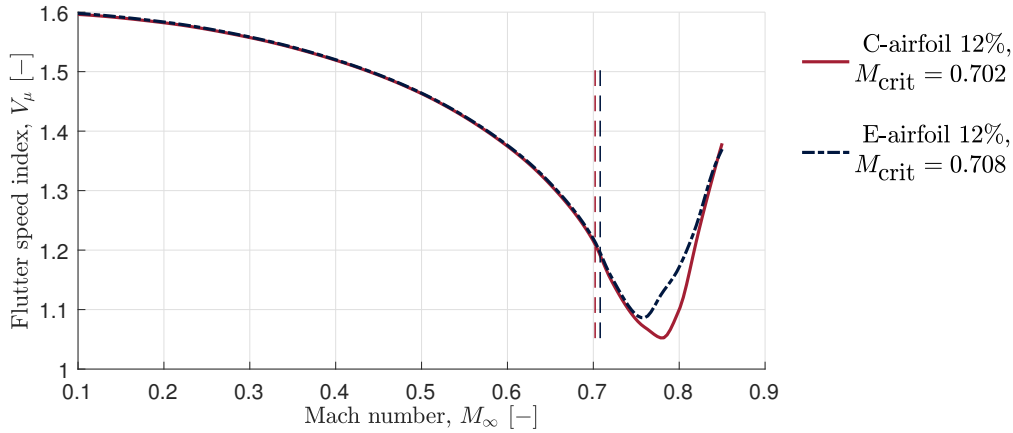


Figure 19. Comparison of flutter boundary between the E-airfoil and C-airfoil, both 12% thick at $c_{l_0} = 0.6$. For this case $\mu = 40$, $\omega_{\theta}/\omega_h = 0.5$, $r_{\theta}^2 = 2.5$, $x_{ea}/c = -0.3$, $x_{cg}/c = 0.35$.

are calibrated using Dynamic Mode Decomposition. The approach has been demonstrated by fitting the model to unsteady CFD simulations for a pitching and heaving RAE2822 in subsonic and transonic flow. The calibrated model is then evaluated for its ability to predict the unsteady response over a relatively wider range of flows than was used in the calibration set. The calibrated model is also used to investigate the effect of compressibility on the flutter boundary of an RAE2822 airfoil. The influence of baseline lift coefficient, freestream Mach number, and airfoil thickness on the flutter boundary is investigated using the resulting low-order model. Finally, the accuracy of the low-order model is confirmed for a classic flutter test problem from the literature.

Acknowledgements

This work was supported in part by the NASA LEARN program grant number NNX14AC73A and the SUTD-MIT International Design Center.

References

¹Bradley, M. K. and Dronev, C. K., “Subsonic Ultra Green Aircraft Research: Phase I Final Report,” Tech. Rep. NASA/CR2011-216847, National Aeronautics and Space Administration (NASA), Boeing Research & Technology, Hunting-

ton Beach, California, April 2011.

²Kennedy, G. J., Kenway, G. K. W., and Martins, J. R. R. A., “Towards Gradient-Based Design Optimization of Flexible Transport Aircraft with Flutter Constraints,” *15th AIAA/ISSMO Multidisciplinary Analysis and Optimization Conference, Atlanta, Georgia*, June 16–20 2014.

³Mallik, W., Kapania, R. K., and Schetz, J. A., “Multidisciplinary Design Optimization of Medium-Range Transonic Truss-Braced Wing Aircraft with Flutter Constraint,” *54th AIAA/ASME/ASCE/AHS/ASC Structures, Structural Dynamics, and Materials Conference*, April 8–11 2013.

⁴Bendiksen, O. O., “Review of Unsteady Transonic Aerodynamics: Theory and Applications,” *Progress in Aerospace Sciences*, Vol. 47, No. 2, 2011, pp. 135–167.

⁵Mykytow, W. J., “A Brief Overview of Transonic Flutter Problems,” *Unsteady Airloads in Separated and Transonic Flow, AGARD-CP-226, North Atlantic Treaty Organization*, 1977.

⁶Farmer, M. G. and Itanson, P. W., “Comparison of Supercritical and Conventional Wing Flutter Characteristics,” Tech. Rep. TM X-72837, National Aeronautics and Space Administration (NASA), Langley Research Center, Hampton, Virginia, May 1976.

⁷Kholodar, D. B., Thomas, J. P., Dowell, E. H., and Hall, K. C., “Parametric Study of Flutter for an Airfoil in Inviscid Transonic Flow,” *Journal of Aircraft*, Vol. 40, No. 2, 2003, pp. 303–313.

⁸Kholodar, D. B., Dowell, E. H., Thomas, J. P., and Hall, K. C., “Improved Understanding of Transonic Flutter: a Three-Parameter Flutter Surface,” *Journal of Aircraft*, Vol. 41, No. 4, 2004, pp. 911–917.

⁹Reddy, T. S. R., Srivastava, R., and Kaza, K. R. V., “The Effects of Rotational Flow, Viscosity, Thickness, and Shape on Transonic Flutter Dip Phenomena,” *29th AIAA/ASCE/AHS/ASC Structures, Structural Dynamics and Materials Conference, Williamsburg, Virginia*, April 18–20 1988.

¹⁰Theodorsen, T., “General Theory of Aerodynamic Instability and the Mechanism of Flutter,” Tech. Rep. NACA-TR-496, National Aeronautics and Space Administration (NASA), Langley Aeronautical Lab, Hampton, Virginia, January 1935.

¹¹Amiet, R. K., “Compressibility Effects in Unsteady Thin-Airfoil Theory,” *AIAA Journal*, Vol. 12, No. 2, 1974, pp. 252–255.

¹²Osborne, C., “Unsteady Thin-Airfoil Theory for Subsonic Flow,” *AIAA Journal*, Vol. 11, No. 2, 1973, pp. 205–209.

¹³Miles, J. W., “On the Compressibility Correction for Subsonic Unsteady Flow,” *Journal of the Aeronautical Sciences*, 1950.

¹⁴Possio, C., “L’Azione Aerodinamica sul Profilo Oscillante in un Fluido Comprimibile a Velocità Iposonora,” *L’Aerotecnica*, Vol. 18, 1938, pp. 441–459.

¹⁵Balakrishnan, A. V., “Unsteady Aerodynamics – Subsonic Compressible Inviscid Case,” Tech. Rep. NASA/CR-1999-206583, National Aeronautics and Space Administration (NASA), Dryden Flight Research Center, Edwards, California, August 1999.

¹⁶Lin, J. and Iliff, K. W., “Aerodynamic Lift and Moment Calculations Using a Closed-Form Solution of the Possio Equation,” Tech. Rep. NASA/CR-2000-209019, National Aeronautics and Space Administration (NASA), Dryden Flight Research Center, Edwards, California, April 2000.

¹⁷Garrick, I. E., “Bending-Torsion Flutter Calculations Modified by Subsonic Compressibility Corrections,” Tech. Rep. TN 1034, National Advisory Committee for Aeronautics, Langley Memorial Aeronautical Laboratory, Langley Field, Virginia, May 1946.

¹⁸Lomax, H., Heaslet, M. A., Fuller, F. B., and Sluder, L., “Two- and Three-Dimensional Unsteady Lift Problems in High-Speed Flight,” Tech. Rep. NACA TN 1077, National Advisory Committee for Aeronautics (NACA), 1952.

¹⁹Stahara, S. S. and Spreiter, J. R., “Development of a Nonlinear Unsteady Transonic Flow Theory,” Tech. Rep. NASA/CR-2258, National Aeronautics and Space Administration (NASA), Langley Research Center, Hampton, Virginia, June 1973.

²⁰Isogai, K., “On the Transonic-dip Mechanism of Flutter of a Sweptback Wing,” *AIAA Journal*, Vol. 17, No. 7, 1979, pp. 793–795.

²¹Dowell, E., “A Simplified Theory of Oscillating Airfoils in Transonic Flow – Review and Extension,” *18th AIAA/ASCE/AHS/ASC Structures, Structural Dynamics and Materials Conference*, San Diego, California, March 21–23 1977.

²²Nixon, D., “Perturbation of a Discontinuous Transonic Flow,” *AIAA Journal*, Vol. 16, No. 1, 1978, pp. 47–52.

²³Leishman, J. G. and Nguyen, K. Q., “State-Space Representation of Unsteady Airfoil Behavior,” *AIAA Journal*, Vol. 28, No. 5, 1990, pp. 836–844.

²⁴Benner, P., Gugercin, S., and Willcox, K., “A Survey of Projection-Based Model Reduction Methods for Parametric Dynamical Systems,” *SIAM Review*, Vol. 57, No. 4, 2015, pp. 483–531.

²⁵Thomas, J. P., Dowell, E. H., and Hall, K. C., “Modeling Viscous Transonic Limit Cycle Oscillation Behavior using a Harmonic Balance Approach,” *Journal of Aircraft*, Vol. 41, No. 6, 2004, pp. 1266–1274.

²⁶Sirovich, L., “Turbulence and the Dynamics of Coherent Structures. Part 1: Coherent Structures,” *Quarterly of Applied Mathematics*, Vol. 45, No. 3, October 1987, pp. 561–571.

²⁷Berkooz, G., Holmes, P., and Lumley, J., “The Proper Orthogonal Decomposition in the Analysis of Turbulent Flows,” *Annual Review of Fluid Mechanics*, Vol. 25, 1993, pp. 539–575.

²⁸Dowell, E. H. and Hall, K. C., “Modeling of Fluid-Structure Interaction,” *Annual Review of Fluid Mechanics*, Vol. 33, No. 1, 2001, pp. 445–490.

²⁹Silva, W. A., “Application of Nonlinear Systems Theory to Transonic Unsteady Aerodynamic Responses,” *Journal of Aircraft*, Vol. 30, No. 5, 1993, pp. 660–668.

³⁰Lucia, D. J., Beran, P. S., and Silva, W. A., “Reduced-Order Modeling: New Approaches for Computational Physics,” *Progress in Aerospace Sciences*, Vol. 40, No. 1, 2004, pp. 51–117.

³¹Thomas, J. P., Dowell, E. H., and Hall, K. C., “Three-Dimensional Transonic Aeroelasticity using Proper Orthogonal Decomposition-Based Reduced-Order Models,” *Journal of Aircraft*, Vol. 40, No. 3, 2003, pp. 544–551.

- ³²Lieu, T. and Farhat, C., “Adaptation of Aeroelastic Reduced-Order Models and Application to an F-16 Configuration,” *AIAA Journal*, Vol. 45, No. 6, 2007, pp. 1244–1257.
- ³³Dowell, E., Edwards, J., and Strganac, T., “Nonlinear Aeroelasticity,” *Journal of Aircraft*, Vol. 40, No. 5, 2003, pp. 857–874.
- ³⁴Drela, M., “ASWING 5.99 Technical Description – Steady Formulation,” 2015.
- ³⁵Drela, M., “ASWING 5.99 Technical Description – Unsteady Extension,” 2015.
- ³⁶Mateescu, D., “Theoretical Solutions for Unsteady Compressible Subsonic Flows Past Oscillating Rigid and Flexible Airfoils,” *Mathematics in Engineering, Science & Aerospace (MESA)*, Vol. 2, No. 1, 2011.
- ³⁷Oskam, B., “Transonic Panel Method of the Full Potential Equation applied to Multicomponent Airfoils,” *AIAA Journal*, Vol. 23, No. 9, Sep 1985.
- ³⁸Weissinger, J., “Über die Auftriebsverteilung von Pfeilflügeln,” Tech. Rep. 1553, Zentrale für wissenschaftliches Berichtswesen der Luftfahrtforschung des Generalluftzeugmeisters (ZWB), Berlin-Adlershof, February 1942.
- ³⁹Weissinger, J., “The Lift Distribution of Swept-Back Wings,” Tech. Rep. 1120, National Advisory Committee for Aeronautics (NACA), Washington, March 1947.
- ⁴⁰Drela, M. and Giles, M. B., “Viscous-Inviscid Analysis of Transonic and Low Reynolds Number Airfoils,” *AIAA Journal*, Vol. 25, No. 10, 1987, pp. 1347–1355.
- ⁴¹Drela, M., “Design and Optimization Method for Multi-Element Airfoils,” *AIAA/AHS/ASCE Aerospace Design Conference*, Irvine, California, February 16–19 1993.
- ⁴²Drela, M., “A Users Guide to MSES,” Tech. Rep. 3.05, Cambridge, Massachusetts, July 2007.
- ⁴³Ashley, H. and Landahl, M., *Aerodynamics of wings and bodies*, Addison-Wesley Publishing Company, Reading, Massachusetts, 1965.
- ⁴⁴Bisplinghoff, R. L., Ashley, H., and Halfman, R. L., *Aeroelasticity*, Dover Publications, New York, 1996.
- ⁴⁵Dowell, E. H., *A modern course in aeroelasticity*, Springer, Cham, 2014.
- ⁴⁶Schmid, P. J., “Dynamic mode decomposition of numerical and experimental data,” *Journal of Fluid Mechanics*, Vol. 656, 2010, pp. 5–28.
- ⁴⁷Proctor, J. L., Brunton, S. L., and Kutz, J. N., “Dynamic Mode Decomposition with Control,” *SIAM Journal on Applied Dynamical Systems*, Vol. 15, No. 1, 2016, pp. 142–161.
- ⁴⁸Al-Saggaf, U. M. and Franklin, G. F., “Model reduction via balanced realizations: an extension and frequency weighting techniques,” *IEEE Transactions on Automatic Control*, Vol. 33, No. 7, 1988, pp. 687–692.
- ⁴⁹Palacios, F., Colonno, M. R., Aranake, A. C., Campos, A., Copeland, S. R., Economon, T. D., Lonkar, A. K., Lukaczyk, T. W., Taylor, T. W., and Alonso, J. J., “Stanford University Unstructured (SU2): An Open-Source Integrated Computational Environment for Multi-Physics Simulation and Design,” *51st AIAA Aerospace Sciences Meeting*, Grapevine, Texas, January 7–10 2013.
- ⁵⁰Jameson, A., “Time Dependent Calculations using Multigrid, with Applications to Unsteady Flows Past Airfoils and Wings,” *10th AIAA Computational Fluid Dynamics Conference*, Honolulu, Hawaii, June 24–26 1991.
- ⁵¹Shewchuk, J. R., “Adaptive precision floating-point arithmetic and fast robust geometric predicates,” *Discrete & Computational Geometry*, Vol. 18, No. 3, 1997, pp. 305–363.
- ⁵²Drela, M., “Integrated Simulation Model for Preliminary Aerodynamic, Structural, and Control-law Design of Aircraft,” *40th Structures, Structural Dynamics, and Materials Conference and Exhibit*, St. Louis, Missouri, April 12–15 1999, pp. 1644–1656.
- ⁵³Isogai, K., “Transonic Dip Mechanism of Flutter of a Sweptback Wing: Part II,” *AIAA Journal*, Vol. 19, No. 9, 1981, pp. 1240–1242.
- ⁵⁴Alonso, J. J. and Jameson, A., “Fully-Implicit Time-Marching Aeroelastic Solutions,” *32nd Aerospace Sciences Meeting & Exhibit*, Reno, Nevada, January 10–13 1994.
- ⁵⁵Thomas, J. P., Hall, K. C., and Dowell, E., “Reduced Order Aeroelastic Modeling using Proper Orthogonal Decompositions,” *International Forum of Aeroelasticity and Structural Dynamics*, Williamsburg, Virginia, 1999.
- ⁵⁶Liu, F., Cai, J., Zhu, Y., Tsai, H., and Wong, A., “Calculation of wing flutter by a coupled fluid-structure method,” *Journal of Aircraft*, Vol. 38, No. 2, 2001, pp. 334–342.
- ⁵⁷Sanchez, R., Kline, H., Thomas, D., Variyar, A., Righi, M., Economon, T., Alonso, J., Palacios, R., Dimitriadis, G., and Terrapon, V., “Assessment of the fluid-structure interaction capabilities for aeronautical applications of the open-source solver SU2.” *Proceedings of the VII European Congress on Computational Methods in Applied Science and Engineering*, 2016.